EPITAXIAL GROWTH OF GaN ON GaN MULTI QUANTUM WELL FOR THE DEEP GREEN LIGHT EMITTING DIODE

SHAMSUL AMIR BIN ABDUL RAIS

UNIVERSITI SAINS MALAYSIA

2022

EPITAXIAL GROWTH OF GaN ON GaN MULTI QUANTUM WELL FOR THE DEEP GREEN LIGHT EMITTING DIODE

by

SHAMSUL AMIR BIN ABDUL RAIS

Thesis submitted in fulfilment of the requirements
for Degree of
Doctor of Philosophy

October 2022

ACKNOWLEDGEMENT

Bismillahirrrahmanirrahim. All praise to Allah Almighty, as for His Grace and Mercy that I can finish this work in form of this thesis. Peace be upon our great Prophet Muhammad as for his guidance that we are able to live on the right path. My most thankful thought and prayers towards both of my parents whom both had passed away, as for the kindness and blessing bringing me up that I am able to here right now. I would like to extend my gratitude to my supervisor, Professor Dr. Zainuriah Hassan who help, guided, support, and encourage me throughout my period of research. Without her lead and wise words, none of this effort would be fruitful.

I would also like to thank my fellow researchers in Universiti Malaya, headed by my co-supervisor Dr. Ahmad Shuhaimi, and his team, Nazri, Yusnizam, Fadil, Alif, Sobri, Najihah, Anas, Omar, and Adreen for their warm welcome and relentless support when I was working in their lab.

My thanks also go to my irreplaceable colleagues in Universiti Sains Malaysia, Ikram, who if without him, I would be totally lost on the campus. Not to forget Esmed, Ezzah, Dr. Norzaini, En Anas, Sauffi, Ann, and Waheeda, who were my best research companions in USM.

Last but not least, I would like to thank my siblings and their kids who were always there for me, and 2 of my best UniMAP friends, Fairus and Natashah.

TABLE OF CONTENTS

ACKNOWLEDGEMENT .... **ii**

TABLE OF CONTENTS .... **iii**

LIST OF TABLE .... **vii**

LIST OF FIGURES .... **viii**

LIST OF SYMBOLS .... **xiii**

LIST OF ABBREVIATIONS .... **xiv**

ABSTRAK .... **xvi**

ABSTRACT .... **xviii**

CHAPTER 1 INTRODUCTION **1**

1.1 Overview 1

1.2 Motivation and problem statement. 2

1.3 Project scope. 4

1.4 Research objectives 4

1.5 Research originality. 4

1.6 Thesis outline. 6

CHAPTER 2 LITERATURE REVIEW **8**

2.1 Overview of semiconductor material 8

2.2 GaN crystal as an optoelectronic material 9

2.3 Lattice mismatch and crystal defect. 13

2.3.1 Point defect..14

2.3.2 Line defect..15

2.3.3 Grain boundaries 17

2.3.4 Inversion domains and antiphase 18

2.4 Substrate materials..19

2.5 Current techniques to grow III-V crystals. 21

2.5.1 Plasma assisted molecular beam epitaxy (PAMBE) 21

2.5.2 Reactive magnetron sputtering..22

2.5.3 Metal-organic chemical vapor deposition (MOCVD)........25

2.5.4 Pulsed laser deposition (PLD). 26

2.6 MOCVD growth techniques. 29

2.7 MOCVD and GaN crystal growth. 34

2.8 The P-I-N diode and the MQW. 36

2.9 The full LED structures 38

2.10 Recent progress in green LED studies...41

2.11 The Vegard's law...43

2.12 Summary..43

CHAPTER 3 METHODOLOGY..45

3.1 Overview 45

3.2 Structure and growth of multi quantum well (MQW)......................46

3.3 Structure and growth of full GaN-on-GaN LED 50

3.3.1 Sample A: the basic green LED 52

3.3.2 Sample B: the LED with indium pre-flow. 54
3.3.3 Sample C: the LED with indium pre-flow and higher nitrogen in III-V ratio. 57
3.3.4 Sample D: the LED with indium pre-flow and no AlGaN cap. 59
3.3.5 Sample E: the LED with indium pre-flow, higher nitrogen in III-V ratio, and no AlGaN cap. 61
3.3.6 Summary of all LED grown. 63
3.3.7 Sample preparation for transmission electron microscopy characterization. 63
3.3.8 The sample preparation for electrical characterization. 65
3.4 Summary 66
CHAPTER 4 RESULTS AND DISCUSSIONS 67
4.1 The MQW results 67
4.1.1 Photoluminescence of the MQW 67
4.1.2 XRD characterization of MQW 68
4.1.3 Atomic force microscopy (AFM) of the MQW. 72
4.2 The full deep green light emitting diodes (LED) results 74
4.2.1 The full LED photoluminescence (PL) results 76
4.2.2 The full LED XRD characterizations 82
4.2.3 Vegard’s law of wavelength shift 101
4.2.4 The full LED cross-sectional image 104

4.2.5 The atomic force microscopy (AFM) surface morphology of the full LED 107

4.2.6 The field emission scanning electron microscopy (FESEM) surface morphology of full LED 116

4.2.7 Hall effect measurement of the full LED 120

4.2.8 The current-voltage characteristic of the full LED 123

4.2.9 The electroluminescence (EL) spectrum of the full LED 125

4.3 Summary 129

CHAPTER 5 CONCLUSIONS AND FUTURE WORKS 133

5.1 Conclusions 133

5.2 Future works 135

REFERENCES 138

LIST OF PUBLICATION160S

LIST OF INTERNATIONAL CONFERENCE161S

LIST OF TABLE

Page

Table 2.1 Mechanical and thermal properties of gallium nitride (GaN) ...12

Table 2.2 Summary of MOCVD and GaN crystal growth 35

Table 3.1 Details of PSS substrate properties...50

Table 3.2 Summary of Ga:In ratio in all of MQW samples 50

Table 3.3 Details of GaN substrate properties..51

Table 3.4 The table of samples and alterations undergone........................63

Table 4.1 The AFM roughness RMS value of all the MQW samples.......72

Table 4.2 The table of samples and alteration undergone 81

Table 4.3 The concentration of indium in the $In_xGa_{1-x}N$ layer from omega2θ simulation plot calculation......................................101

Table 4.4 The concentration of indium in the $In_xGa_{1-x}N$ layer from omega2θ simulation plot calculation......................................103

Table 4.5 The change of indium concentration in the $In_xGa_{1-x}N$ layer from Vegard's law calculation. 103

Table 4.6 The summary of AFM results of all samples. 116

Table 4.7 The summary of Hall effect characterization of all the LED samples 122

Table 4.8 The summary of PL and EL characterization of all the LED samples 129

LIST OF FIGURES

Page

Figure 2.1 Bandgap energy as a function of lattice constant[23] 10

Figure 2.2 Common types of point defects in the crystal[66].....................16

Figure 2.3 The types of dislocation modes in the wurtzite structure (a) edge and (b) screw dislocation. Diagram (c) shows the line direction relation to Burgers vector[65]. 16

Figure 2.4 Inversion domain boundary in GaN[74]...................................19

Figure 2.5 The schematic diagram of PAMBE system[81]. 22

Figure 2.6 Schematic diagram of an RF sputter[85]. 24

Figure 2.7 The side view of the inlet flow of a MOCVD[88]. 26

Figure 2.8 The illustration of the PLD inner chamber[89]. 27

Figure 2.9 The schematic of crystal layer growth in MOCVD[21]............30

Figure 2.10 LED with a single quantum well..40

Figure 2.11 LED with simple MQW 41

Figure 3.1 The methodology and characterization flow 46

Figure 3.2 The GaN crystal orientation in form of hexagonal coordinates. Gallium atoms are shaded grey and nitrogen atoms are shaded blue[102]...47

Figure 3.3 The structure of the MQW. 49

Figure 3.4 The picture of a PSS substrate..49

Figure 3.5 The picture of a GaN substrate 52

Figure 3.6 The basic structure of the full LED of a) sample A , b) samples B and C, and c) samples D and E 54

Figure 3.7 Image of sample A trench after FIB milling under FESEM 64

Figure 3.8 Sample after top side removed and applied with indium contact..65

Figure 3.9 Sample preparation for Hall Effect characterization. 66

Figure 4.1 Photoluminescence spectrum of the MQW of all samples........68

Figure 4.2 The X-ray rocking curve(XRC) plot of the MQW of all samples. 69

Figure 4.3 The omega2θ scan plot of the MQW of all samples. 71

Figure 4.4 AFM surface topography of of the MQW of all samples..........73

Figure 4.5 The structure of the LED without the indium pre-flow.............75

Figure 4.6 The structure of the LED with the indium pre-flow..................75

Figure 4.7 The PL result of sample A..77

Figure 4.8 The PL result of sample B..77

Figure 4.9 The PL result of sample C..78

Figure 4.10 The PL results of sample D...79

Figure 4.11 The PL results of sample E..80

Figure 4.12 The summarized PL results of sample A,B,C,D and E 82

Figure 4.13 The XRD omega2θ result of sample A after annealing 83

Figure 4.14 The XRD rocking-curve result of sample A after annealing.....84

Figure 4.15 The XRD omega2θ result of sample B before annealing..........85

Figure 4.16 The XRD rocking-curve result of sample B before annealing..85

Figure 4.17 The XRD omega2θ result of sample B after annealing.............86

Figure 4.18 The XRD rocking-curve result of sample B after annealing.....87

Figure 4.19 The XRD omega2θ result of sample C before annealing..........88

Figure 4.20 The XRD rocking-curve result of sample C before annealing..89

Figure 4.21 The XRD omega2θ result of sample C after annealing.............90

Figure 4.22 The XRD rocking-curve result of sample C after annealing.....91

Figure 4.23 The XRD omega2θ result of sample D before annealing..........91

Figure 4.24 The XRD rocking-curve result of sample D before annealing..92

Figure 4.25 The XRD omega2θ result of sample D after annealing 93

Figure 4.26 The XRD rocking-curve result of sample D after annealing.....93

Figure 4.27 The XRD omega2θ result of sample E before annealing..........94

Figure 4.28 The XRD rocking-curve result of sample E before annealing ..95

Figure 4.29 The XRD omega2θ result of sample E after annealing.............96

Figure 4.30 The XRD rocking-curve result of sample E after annealing 96

Figure 4.31 The summary of sample A XRD results, a) the omega2θ and b) the rocking curve plot. 97

Figure 4.32 The summary of sample B XRD results, a) the omega2θ (left) and the rocking curve plot (right) and b) the omega2θ (left) the rocking curve plot (right)..98

Figure 4.33 The summary of sample C XRD results, a) the omega2θ (left) and the rocking curve plot (right) and b) the omega2θ (left) the rocking curve plot (right)..98

Figure 4.34 The summary of sample D XRD results, a) the omega2θ (left) and the rocking curve plot (right) and b) the omega2θ (left) the rocking curve plot (right)..99

Figure 4.35 The summary of sample D XRD results, a) the omega2θ (left) and the rocking curve plot (right) and b) the omega2θ (left) the rocking curve plot (right)..99

Figure 4.36 The transmission electron microscopy (TEM) cross-sectional image of sample A after annealing...104

Figure 4.37 The transmission electron microscopy (TEM) cross-sectional image of sample B before annealing 105

Figure 4.38 The transmission electron microscopy (TEM) cross-sectional image of sample B after annealing 105

Figure 4.39 The combined transmission electron microscopy (TEM) cross-sectional image of sample A after annealing (a), sample B before annealing (b), and sample B after annealing (c)...........106

Figure 4.40 AFM images of sample A after annealing..............................108

Figure 4.41 AFM images of sample B before annealing 109

Figure 4.42 AFM images of sample B after annealing..............................109

Figure 4.43 AFM images of sample C before annealing 110

Figure 4.44 AFM images of sample C after annealing..............................111

Figure 4.45 AFM images of sample D before annealing...........................112

Figure 4.46 AFM images of sample D after annealing..............................112

Figure 4.47 AFM images of sample E before annealing 113

Figure 4.48 AFM images of sample E after annealing 114

Figure 4.49 FESEM surface image of sample A after annealing at 50,000 times magnification. 117

Figure 4.50 FESEM surface images of sample B before (left) and after (right) annealing at 50000 times magnification.......................117

Figure 4.51 FESEM surface images of sample C before (left) and after (right) annealing at 50000 times magnification.......................118

Figure 4.52 FESEM surface images of sample D before (left) and after (right) annealing at 50000 times magnification.......................119

Figure 4.53 FESEM surface images of sample E before (left) and after (right) annealing at 50000 times magnification.......................119

Figure 4.54 The I-V curves of all the LED samples. 124

Figure 4.55 The electroluminescence spectra of samples A, B, and C.......126

Figure 4.56 The picture of LED samples A, B, and C................................129

LIST OF SYMBOLS

b	Magnitude of the ***b*** vector
β	Full half-width maximum (FHWM) value in radian
C_{11}	Elastic constant
E_g	Bandgap energy
$\boldsymbol{g}$	Diffraction vector of XRC
H	Vickers hardness
K_c	Fracture toughness
K_g	Mass transport coefficient
P_{eqMO}	Equilibrium pressure of the metalorganic vapor
ρ	Dislocation
r	Growth rate
V_D	Diffusion voltage
V_{th}	Threshold voltage

LIST OF ABBREVIATIONS

2DEG	Two-dimension electron gas
AFM	Atomic force microscopy
CTE	Coefficient of thermal expansion
CVD	Chemical vapor deposition
DC	Direct current
DL	Deep level emission
EBL	Electron blocking layer
EL	Electroluminescence
FESEM	Field emission scanning electron microscopy
FIB	Focused ion beam
FWHM	Full width at half maximum
LED	Light-emitting diode
MQW	Multi-quantum well
MOCVD	Metal-organic chemical vapor deposition
PAMBE	Plasma assisted molecular beam epitaxy
PL	Photoluminescence
PLD	Pulsed laser deposition
PSS	Patterned sapphire substrate
QW	Quantum well

RF	Radio frequency
RMS	Root mean square
SCCM	Standard cubic centimeters per minute
SLM	Standard cubic per minute
TD	Threading dislocation
TEM	Transmission electron microscopy
TEG	Triethylgallium
TMA	Trimethylaluminum
TMG	Trimethylgallium
TMI	Trimethylindium
UV	Ultraviolet

PENUMBUHAN EPITAKSI TELAGA KUANTUM BERBILANG GaN ATAS GaN BAGI DIOD PEMANCAR CAHAYA HIJAU TUA

ABSTRAK

Kerja ini memberikan tumpuan kepada usaha untuk fabrikasi diod pemancar cahaya (LED) hijau tua. Untuk permulaan, telaga kuantum pelbagai (MQW) yang dijangka mampu untuk memancarkan cahaya hijau tua telah direkabentuk dan difabrikasi. Terlebih dahulu MQW ditumbuhkan di atas substrat nilam berpaten kerana ia mempunyai lapisan nukleasi dan kepadanan kekisi paling hampir dengan substrat gallium nitride (GaN). Penumbuhan 6 pasang lapisan GaN/ $In_xGa_{1-x}N$ yang berketebalan 12.16/3.35 nm telah berjaya dilakukan. MQW tersebut mempunyai kualiti kristal yang baik dengan kecacatan rendah walaupun nisbah indium adalah 9 kali ganda jumlah galium telah diperolehi. Kajian terdahulu menunjukkan kandungan indium yang tinggi dalam penumbuhan kristal GaN akan menghasilkan ketegangan kristal tinggi namun tanda-tanda tersebut tidak kelihatan. MQW ini kemudian dimasukkan ke dalam struktur LED penuh. LED ini ditumbuhkan di atas substrat GaN. LED yang terhasil mempunyai kualiti kristal yang baik dengan dislokasi kristal 8.7×10^7 cm^{-2}. Spektrum fotoluminesen (PL) memberikan keputusan yang baik iaitu 568 nm yang berada dalam kawasn hijau tua. Namun, peranti ini perlu disepuhlindap untuk mengaktifkan jenis-p, dan anjakan biru panjang gelombang telah berlaku dengan banyak iaitu 45nm selepas proses penyepuhlindapan. Ini membuatkan teknik pra-alir indium diperkenalkan untuk penumbuhan sampel-sampel LED berikutnya. Teknik ini bukan sekadar menghalang anjakan biru LED tetapi juga berjaya menunjukkan anjakan merah sebanyak 3nm bagi spektrum PL untuk sampel yang terbaik. Puncak PL menganjak dari 548 nm ke 551 nm. Lapisan mendadak MQW berjaya dikekalkan seperti yang diperhatikan dari imej keratan rentas mikroskopi pancaran electron (TEM). Tambahan lagi, imej TEM menunjukkan kontras MQW yang lebih baik lantas membuktikan bahawa teknik pra-alir indium memperbaiki MQW selepas peyepuhlindapan. Kualiti permukaan bagi kesemua sampel adalah baik, dengan nilai RMS AFM antara 1-8 nm, dengan kekasaran rendah, tiada lubang dan nilai lengkungan yang sangat kecil. Semua ini dipercayai disebabkan oleh pengguaan substrat GaN. Lengkungan arus-voltan (I-V) menunjukkan LED dengan struktur biasa mempunyai separa-ambang tidak mendadak, manakala LED tanpa lapisan penampan elektron (EBL) menunjukkan separa ambang mendadak. Ini menyebabkan LED tanpa struktur EBL tidak menyala. LED yang melalui proses pra-alir mempunyai puncak elektroluminesen (EL) menganjak ke merah berbanding dengan PL sementara sampel tanpa pra-alir menunjukkan anjakan biru, berpunca dari kesan kuantum-terkurung Stark, seperti dilaporkan di dalam lain-lain laporan. Sampel LED terbaik mempunyai spektrum EL pada 559 nm, yang mana mencapai sasaran kerja ini.

EPITAXIAL GROWTH OF GaN ON GaN MULTI QUANTUM WELL FOR THE DEEP GREEN LIGHT EMITTING DIODE

ABSTRACT

This work has focused on the effort of fabricating the deep green light emitting diode (LED). First, the multi-quantum well (MQW) that was expected to be able to emit a deep green wavelength was designed and fabricated. The MQW was first grown on a patterned sapphire substrate due to nucleation layer and lattice match which are nearest to the gallium nitride (GaN) substrate. The growth of six pairs of GaN/ $In_xGa_{1-x}N$ layer that has 12.16/3.35 nm thickness was successfully carried out. The MQW has low crystal defect even when the indium ratio for $In_xGa_{1-x}N$ layer growth was 9 times more than gallium. Previous research shows that a high indium ratio in GaN crystal growth would yield high strain but none of these have been observed. The MQW was later inserted into the full LED structure. The LED was grown on the GaN substrate. The resulting LED has good crystal quality, with dislocation of $8.7 \times 10^7 cm^{-2}$. The photoluminescence (PL) spectrum also gives a good result, 568 nm which is in the deep green region. However, the device needed to be annealed to activate the p-type, and the wavelength blue-shifted greatly, 45nm after the annealing process. This prompted the introduction of the indium pre-flow technique to the later growth of the LED samples. The technique not only suppressed the blue shift of the LED but also succeeded in the red shift, around 3nm of the PL spectrum for the best sample. The PL peak shifted from 548 nm to 551 nm. The abruptness of the MQW was maintained as observed by transmission electron microscopy (TEM) cross section image. Further, the TEM image also demonstrated that the contrast of the MQW layer improves, thus showing that the indium pre-flow technique improves the MQW after annealing. The surface quality of all the samples is good, with AFM RMS values between 1-8 nm, with low roughness, no pits, and very small bowing. All of these attributes are believed as the result of using GaN as the substrate. The current voltage (I-V) curve shows that the normal structure LED has a non-abrupt sub-threshold, while LED samples with no electron blocking layer (EBL) have an abrupt sub-threshold. This resulted in no light-up for the samples with no EBL. The samples that have the indium pre-flow has their electroluminescence (EL) wavelength red shifted compared to PL, while the LED sample without the indium pre-flow blue shifted, as a result of quantum-confined Stark effect as reported in previous reports. The best LED sample has an EL spectrum of 559nm, which achieved the target of this work.

CHAPTER 1

INTRODUCTION

1.1 Overview

The green light emitting diode (LED) has been one of the main focuses of solid-state lighting research. Green LED has good lumens per watt efficacy which by itself can be an incandescent light source with low current consumption[1]. This makes green LEDs perfect for illumination and lighting. Green LED also improved color rendering index[2] in the process of making white light LED. Light in this range also causes a maximum luminous sensation in the human eye[3] and is therefore advantageous for many potential uses. The green light, especially in the deep green region, at a wavelength around 530~570 nm shows better results in data delivering devices, which makes it a popular candidate for Light Fidelity (Li-Fi) system[4]. For these reasons, the research and studies to broaden the LED emission wavelength range have become one of the main targets of solid-state lightning generally[5].

Most of the previous work shows the GaN crystal growth on other semiconductor substrates such silicon, sapphire, or patterned sapphire substrate (PSS). The problems with these substrates are as the diameter of the sample increase, the substrate bow after the epitaxial process increase[6], [7]. This bow gives the deformity in crystal structure such as crack, line dislocation, and void pits (v-pits) at the surface of the samples grown. Further processes after the growth, such as annealing and dry etching worsen this scenario. These crystal defects affect the performance of the LED and all the electronic devices general[8].

Even though studies to overcome these problems have been done and countermeasure step has been introduced, such as the implementation of multi-layer[9],

[10] within the GaN device structure, the resulting samples still show some small defects. These small defects might be permissible in other electronic devices, but for LED which has nanostructure, which is the multi-quantum well (MQW), the crystal defect needs to be minimized.

The GaN substrate provides homogenous growth, which will reduce the problems such as crystal defects and bowing problems significantly. In addition to this, the physical and chemical properties of the substrates and the actual LED layers above are the same, thus make it easier to tune the output of the final product. Thus, the GaN substrate was chosen for the full LED growth.

1.2 Motivation and problem statement.

The main motivation of this work is to fabricate the deep green LED on GaN substrate. To achieve such, first, MQW that emits the green light was needed. This LED must have a quite high indium concentration compared to the blue LED, and the optimum growth condition must be found to incorporate as much indium as needed while maintaining the crystal quality to avoid upcoming problems in emission such as broad-spectrum and dual peaks spectrum.

The problem of incorporating more indium within the MQW was also not only dependent on how indium flow during the growth, but also the temperature and the pressure chamber during the growth. InN has a very low nucleation temperature 350°C so preferably needed low temperature to incorporate into the MQW, in turn crystal strain would increase, and effect the spectrum quality. Finding the optimum pressure was also crucial since higher pressure means more molecules would hit the surface of the substrate, thus increasing reaction, but too high pressure might disturb the precursor chemical flow across the surface of the substrate. Whatever the growth parameters set, the important case was the resulting MQW crystal has the most indium incorporated and maintain good crystal quality.

The other concern is to increase the intensity of the LED. The intensity can be increased by thickening the active layers in the MQW, but by doing so, the possibility of crystal defects due to strain and stress phenomena increases.

The last major problem, which will become the main novelty when tackled, is the indium out diffuse when annealed after the growth ended. The p-type of the LED needed to be annealed to be activated, to remove the hydrogen species that came as the gas carrier in the epitaxy growth process[11], [12]. During this process, the indium, which has a low melting point tends to out diffuse from the MQW, shifting its wavelength towards the blue region.

To counter the first problem, the first novelty would be to apply the appropriate ratio on the Ga: In ratio during the MQW growth phase and optimizing the chamber pressure and the MQW growth temperature to obtain high indium content with high crystal quality MQW.

A thinner $In_xGa_{1-x}N$ active layer was proposed in the MQW, which is 2nm, and in turn, increase the number of pairs in MQW to six pairs to counter the intensity concern. The extra pairs will enable the MQW to have more emitting layers, thus maintaining the brightness of the LED without compensating for the spectrum bandwidth.

Finally, the last novelty in this project was to counter the indium out diffuse from MQW, which would be the indium pre-flow technique. This will be elaborately discussed in the later chapters.

1.3 Project scope.

In this work, the epitaxial growth of deep green LED on gallium nitride (GaN) was demonstrated. All the growth process was done in the metal-organic chemical vapor deposition (MOCVD). The parameters such as precursor chemical flow, reaction chamber pressure, and the temperature were controlled to achieve the structure and the attributes of the samples. The MQW was grown on PSS to study the indium intake in the MQW layers and its spectrum emission and the crystal quality. The MQW then was integrated into the full LED device, and aspects such as indium out-flow from the MQW are studied other than the spectrum and the crystal quality. The deep green LED can be produced by the tuning of the indium content within the MQW and the alteration of the LED structure. The emissions of both photoluminescence (PL) and electroluminescence (PL) were compared and studied.

1.4 Research objectives

The main objectives of this research are

1. To grow multi-quantum well (MQW) epitaxial structures that would be able to emit deep green wavelength.
2. To grow a full light emitting diode (LED) device structure that emits a deep green light.
3. To study and investigate the behavior of the indium content within the full LED device MQW and their effects on the wavelength and structural change.

1.5 Research originality.

The originality of this research work featured by these criteria:

1. Temperature growth for MWQ was set higher than the usual temperature for high indium content layers, and the active layers were grown at the thinnest

thickness. InN has a very low nucleation temperature, around 350°C[13]. The temperature set in previous study around 730°C for InGaN MQW layers gave the output wavelength of 525nm with low indium incorporation, 18.2%. It was not enough to reach deep green wavelength region[14]. Previous studies that gave output in deep green region ~540nm used a very low MQW growth temperature, 600°C[15], which might bring to other problems due to low crystal quality. In this study, 700°C was used as the growth temperature for MQW with output wavelength in the deep green region.

2. The number of MQW pairs was increased and the indium: galium ratio was optimized to achieve brighter LED with a deep wavelength spectrum. MQW layers will also act as multilayers which improved crystal quality[16]. In this study, the number of MQW pairs was set to be 6 pairs. This value was set since undoped GaN layers were sandwiched in between the InGaN active layers, and since GaN has a very wide energy band gap (3.4 eV)[17]. It was hypothesized that electron and holes injected from the n-type and the p-type layers wouldn't be able to overcome the potential barrier and recombined in the active layers if the MQW was too thick, in case if more layers were introduced. The indium:gallium ratio was set at 6:1 after modification of temperatures and pressure of the growth chamber, which resulted in 18-23% of indium incorporated in the MQW.
3. Indium pre-flow was introduced during the full LED growth, which would become the indium-riched n-type layer right beneath the MQW in the device structure.
4. Elaboration of the mechanism of the indium out-diffusion from the MQW layer and its effect on the crystal structure and LED spectrum emission

1.6 Thesis outline.

Chapter 1 presented a brief introduction and overview of deep green LED and its importance and basic properties. The significance and objectives of this work are also highlighted.

Chapter 2 discussed the literature review of GaN as an optoelectronic crystal, the foundation of heterostructure LED, and the current basics of the LED structure. This chapter emphasized the GaN properties as the main material involved in this research. The history of quantum well invention its research progress was also discussed, and how its unique properties were exploited in light emission research. The background of basic LED and its structure improvement to achieve better spectrum emissions were also presented in this chapter.

Chapter 3 provides the methodology of the growth of green MQW and the growth of the full deep green LED device. It includes the selections of the precursor chemical, the reaction involved, and the parameters that were controlled during the growth of the MQW and full LED. The techniques of certain special measurements were also presented in this chapter.

Chapter 4 focused on the results and discussions of this work. The spectrum emission of both MQW and LED samples were observed using PL and EL method, and the results were discussed elaborately around the effect of indium dissipation from the MQW to the wavelength shift of the emissions. To ensure the discussions output was concrete, the results of XRD and TEM images were also taken into account as they provide the structural and compositional perspectives of each fabricated sample. The influence of indium pre-flow, the main novelty within this research was also extensively discussed using these results. The other results such as surface morphology and carrier phenomenon were also presented here. The results were discussed in comparison to other results from other works to verify that both MQW and LED grown in this research were relevant to the current research development.

Finally, **Chapter 5** summarized the conclusion and discussed the possible future works that can be continued from this work.

.

CHAPTER 2

LITERATURE REVIEW

2.1 Overview of semiconductor material

The semiconductor material is described as the material which has the conductivity between the insulator and conductor. This property is determined by its electron valence configuration. The highest band energy of the valance electrons is defined as the valence band while the lowest unfilled band energy is called the conduction bands[18]. In conductors, the conduction and valence bands overlap with each other but are separated by a forbidden gap for insulator and semiconductor materials.

The forbidden gap is also called the energy bandgap and is measured from the top valence band to the bottom of the conduction band. The energy bandgap in semiconductor materials are divided into two types, known as a direct bandgap and indirect bandgap depends on their bands' specific structure[18]. When the lowest energy of the conduction band has the same momentum as the highest energy of the valence band, the semiconductor is classed as a direct bandgap semiconductor. Indium phosphide (InP), gallium arsenide (GaAs), and gallium nitride (GaN) are some examples of direct bandgap semiconductors. Otherwise, when the lowest energy of the conduction band has different momentum as the highest energy of the valence band, the semiconductor is classed as an indirect bandgap semiconductor. Silicon (Si) and germanium (Ge) fall under this type of semiconductor. These differences have a significant impact on their optical properties. The radiative recombination process is relatively fast for a direct bandgap semiconductor since the electron can recombine directly with holes without the need for momentum change. On the other hand, the process is far slower in the indirect bandgap materials because the momentum needs to be facilitated through phonon or lattice vibration[18]. This mechanism creates non-radiative recombination centers and will lead to the loss of energy in the form of heat which will be detrimental to the device performance[19], [20]. This behavior becomes the main reason the direct bandgap materials are preferred in optoelectronic devices.

The incorporation of external impurities called dopants will change their intrinsic characteristics. An atom with an extra valence electron introduced to the host semiconductor is called a donor since the extra electrons become the free electrons in the lattice. These semiconductors are called n-type semiconductors. Contrary, an atom with less electron valance introduced to the host semiconductor is called an acceptor since the unpaired electron in the valance bonding becomes the hole. These semiconductors are called p-type semiconductors. The level of the dopant is proportional to the number of charge carriers of the semiconductor[21]. Silicon (Si) and magnesium (Mg) are the atoms usually used for *n*- and *p*-type dopants for III-V semiconductors[22].

2.2 GaN crystal as an optoelectronic material

To understand GaN as an optoelectronic material, an overview of the material is required. Concerning electronics applications, theoretical electrical and thermal limits of nitride semiconductors as well as their general material and transport properties will determine the advantages of such materials in becoming an optoelectronic device. Among III-V materials, aluminum nitride (AlN) and indium nitride (InN) were considered the best candidates alongside GaN due to their unique bandgap properties. Figure 2.1[23] shows the attributes of these materials. From the figure, it is understood that AlN has the bandgap of 6.2eV and InN has the bandgap of 0.8eV at room temperature

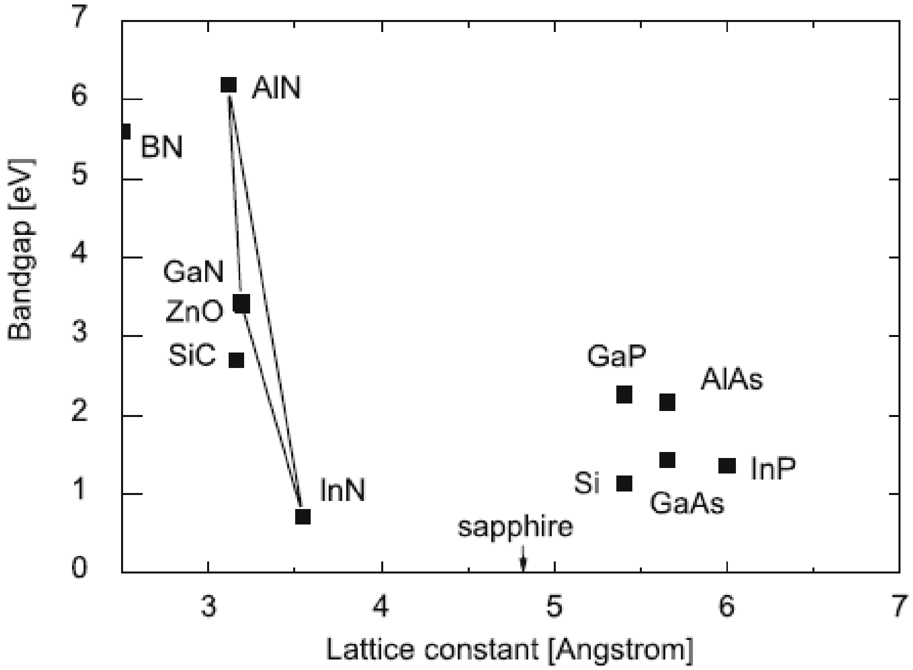

Figure 2.1 Bandgap energy as a function of lattice constant[23]

This gives the III-V materials system a broad range of energies which in turn in terms of emissions wavelength covers from infrared to ultraviolet, which is unchallenged by any other sets of materials. As a result, the wide energy range gives the extremely high bulk breakdown voltage. It can be compensated by changing the material composition of the heterostructures to get low-effective mass and high electron mobility of GaN with $m_n=0.2m_e$ and of InN with $m_n=0.04m_e$[24]. Another big advantage of these materials is due to strong material polar properties, alteration of material composition will result in modifications of polar crystal properties, which gives carrier concentration the interfaces of the material and also the devices[25] [26]. Unlike silicon for which its quality is based on its bulk intrinsic properties and also optimization of the native oxide formation[27] [28].

Of all group III materials that exist, the most popular element to be paired with nitride compound is Al-In-Ga-B[29] [30] [31] [32] [12]. Among these binary nitride compounds, boron nitride is yet to be scientifically explored as a semiconductor material. Silicon, on the other hand is the most popular semiconductor material at the current time, its nitride compound silicon nitride does not have crystalline quality although may be added from time to time as the structure of the device. The properties of silicon nitride and silicon dioxide as optoelectronic material was thoroughly discussed in literature[33]. Three common crystal structures for III-V semiconductors are wurtzite, zincblende, and rock salt. Of these materials, zincblende has not yet found its stable crystal for semiconductor research and rock salt is still yet to play an important part in this field. The focus for semiconductor and optoelectronic devices particularly is the wurtzite crystal structure, which growth is usually done on the *c-plane*. Work on *m-plane* has also been reported in literature[34] [35].

GaN is typically used as the basic materials or the "housing materials" for all device layers for its fast carrier transport and high breakdown voltage. It also can be further grown as a semi-insulating layer or insulating layer which acts as the electron blocking layer (EBL) in full-LED devices.

Table 2.1 shows the mechanical and thermal properties of gallium nitride. Along with the notations given in the value, the mechanical and thermal properties of GaN are extensively discussed in publications[30] [36] [37] [31] [38] [39] [40] [41] [42] [43] [44] [45] [46] [47]. From the tables, it is understood that GaN and its close group III companions in epitaxial growth AlN and InN have nearly the same hardness. The calculations from the table also suggest that GaN has the best elastic constants either in form of temperature dependence or pressure dependence compared to other materials. The bulk modulus B_o of GaN is obtained was 210 GPa. GaN has a linear coefficient of thermal expansion (CTE), in both rooms and much higher temperature. This measurement was done at ambient room temperature and temperature higher than 750°C[48]. The difference in CTE has an impact on epitaxy heterojunction growth, and linear coefficient meant a more uniform and controlled epitaxial growth can be achieved.

Table 2.1 Mechanical and thermal properties of gallium nitride (GaN)

Mass density (g cm^{-3})	6.1[49] [50]
Vickers hardness H (GPa)	12[43] [30]
Fracture toughness K_c(MPa $m^{1/2)}$	0.8[31] [51]
Elastic constant C_{11} (GPa)	390[40]
Coefficient of Thermal Expansion, CTE ($10^{-6}K^{-1}$)	2.8[30] [44]

GaN has dielectric constants of 9.5, which is slightly higher than GaAs. AlN has a value of 8.5 and InN has a value of 15.3. This means the $In_xGa_{1-x}N$ would have a larger resistance in the LED structure. The absorption coefficient of GaN is around 38%, where the absorption peak spectrum is around 3.4 eV[52], the same as its bandgap. This makes GaN is a bad emitter for ultra violet (UV) light instead of its bandgap. Most of this reabsorbed energy would result in phonon electron scattering[53]. The refractive index of GaN is 2.3991[54].

The most reported standard doped bulk GaN carrier concentration is 1 x 10^{17} cm^{-3} for donors and 3 x 10^{16} cm^{-3} for acceptors[48], [52]–[54]. GaN showed low field mobility both in bulk and two-dimension electron gas (2DEG) model. The criteria that influence the mobility of GaN were alloy scattering, acoustic and optical scattering, ionized impurity, and threading dislocation[55], [56]. The low field mobility of free electrons in GaN creates a trade-off with the field transport, with velocity as high as 3 x 10^7 cm s^{-1} [17], [56], comparable to material such as silicon. The 2DEG model in these references suggests that the electrons' drift velocity reduced and relaxation energy increased by the degeneration of electron gas and the hot phonon.

The energy bandgap structure of GaN differs according to the effective mass of electrons and phonons. Several reference[57]–[59] gave a different band structure due to this particular reason, even though all of them applied the Monte Carlo model to calculate the values. The energy bandgap GaN is 3.4 eV for wurtzite and 3.88 eV for zincblende, bandgap energy for AlN is 6.2 eV for wurtzite and 5.94 eV for zincblende, and the bandgap energy for InN is 0.77 eV for wurtzite and 0.75 eV for zincblende. The values for wurtzite are obtained from reference[17] and the values for zincblende are obtained from reference[60]. Since was used the C-plane wurtzite GaN substrate for the LED growth, the values of the wurtzite crystals will be used for the energy bandgap throughout this work.

2.3 Lattice mismatch and crystal defect.

Commonly, every atom is in its specific position at their ideal crystal lattice condition and any deviation of it are known as defects. Defects are predominantly existing in a semiconductor regardless of the degree of material perfection especially at the primary stage of the growth process. The deficiencies in complex semiconductor devices may never be completely unraveled[61].

Following the extortionately high-priced bulk substrate material, the III-V epilayers have experienced a wide variety of defects when be grown on foreign substrates. However, the realization of commercial semiconductor device-based III-V elements has now become possible as the defect densities have been decreased to an adequate level. The following sub-chapter presents a short debate on the most prevalent defects that commonly occurred in every epitaxial growth.

2.3.1 Point defect

Point defects are the most common defect that occurs during the growth of semiconductor materials, where the kinetics and thermodynamics growth has governed their formation. It is basically due to the digression of their lattice from the perfect crystal structure. At an atomic position, a misplaced of atoms called vacancy is the simplest root cause of point defect and leading to the development of an interstitial also known as Frenkel defect. The development of defects energy for line or area is denoted as $N^{1/3}$ and $N^{2/3}$, where N is the number of crystal atoms. So, in thermodynamic equilibrium, these defects are not anticipated. Though this defect should be deemed as a quasi-frozen as it could be at the metastable state due to the slow path of thermodynamic equilibrium, metastable point defects may also exist then. Figure 2.2 illustrates some types of point defects that commonly exist in crystal structures.

The impurity is usually present when a different atom order is populated at an atom site. If the amount of electrons valence is equal to that of the initial atom, it is an isovalent impurity and quasi fits into the bonds. Whereas, a fixed nucleus charge that is compensated by the extra charges to the crystal bonds will occur when the impurity valence is different. Typically, a point defect is followed by a lattice relaxation around the host atoms generate by the missing atom where the next neighbors will move towards the created voids. Here, the relaxation of the lattice relies on the point defect charge status[62].

2.3.2 Line defect

It has been acknowledged that a high threading dislocation density (TDD) will occur if a substrate with highly lattice mismatches is used when growing the III-nitride elements. As for the III-nitride growth at the *c*-plane direction, the threading dislocations (TDs) is categorized into three different modes; *a* + *c* mode or mixed mode with a Burger vector of **b** = 1/3<1 1 $\bar{2}$ 3>, *a*-mode or edge mode with a Burgers vector of **b** = 1/3<1 1 $\bar{2}$ 0>, and *c*-mode or screw mode with a Burger vector of **b** = 1/3<0 0 0 1> [63], [64]. Considering the direction of the dislocations line is parallel to [0 0 0 1], then the dislocation mode for *a* + *c*, *a,* and *c* are mixed, edge, and screw, respectively. At (0 0 1) plane of dislocations line, the *a*-type dislocations with 1/3[$\bar{1}$ $\bar{1}$ 2 0] can be attributed to pure-edge (dislocation line lies parallel to [1 $\bar{1}$ 0 0]) or pure-screw (dislocation line lies parallel to [$\bar{1}$ $\bar{1}$ 2 0]) in the two alternative orientations which are shown in Figure 2.3. So, to accommodate an additional half-plane of material, which becomes imperative when analyzing the transmission electron microscopy (TEM) images with a weak dark field beam, the dislocation line should lie in the (0 0 1)-plane in which to relieve the interfacial mismatch strain[65].

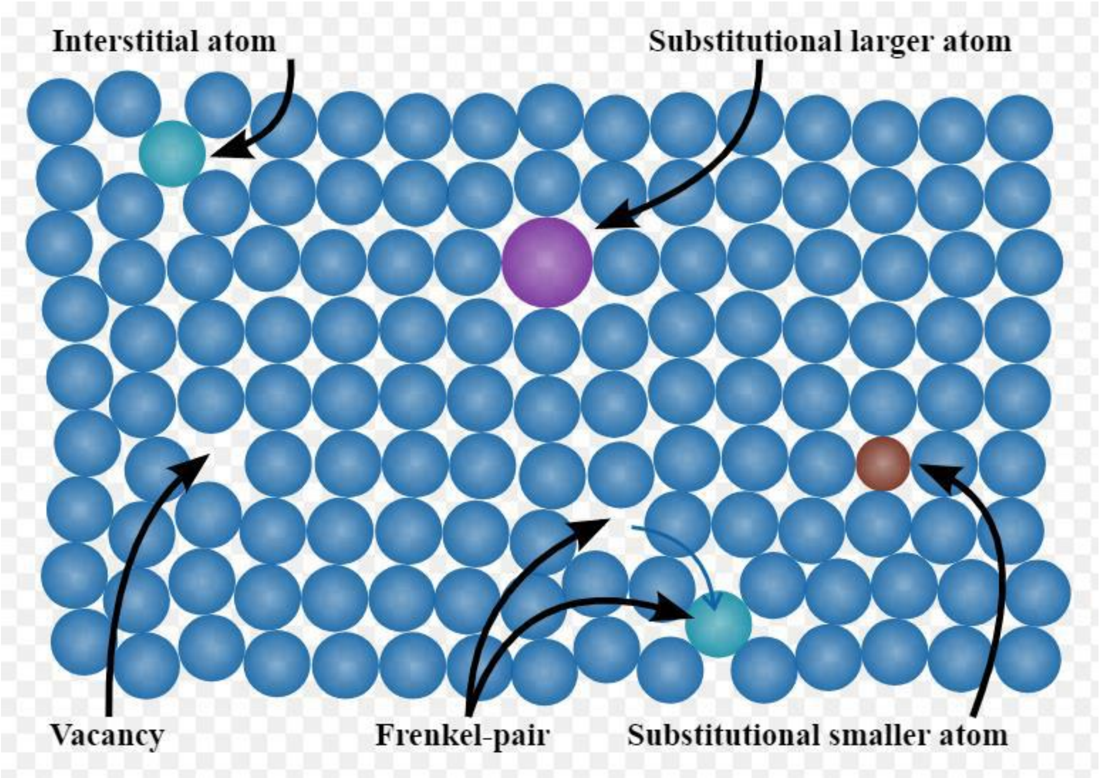
Interstitial atom
Substitutional larger atom
Vacancy
Frenkel-pair
Substitutional smaller atom

Figure 2.2 Common types of point defects in the crystal[66]

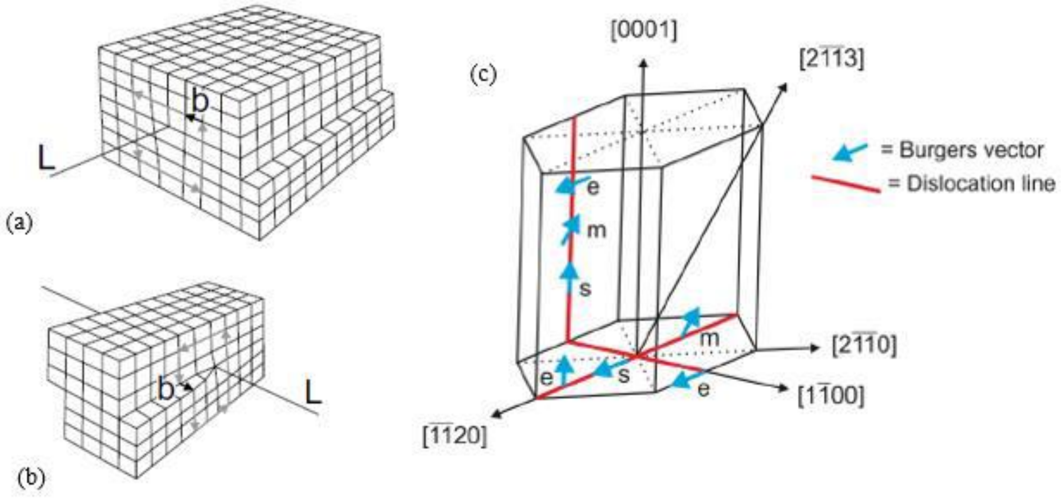
(a)
L
b
(b)
b
L
(c)
$[0001]$
$[2\bar{1}\bar{1}3]$
= Burgers vector
= Dislocation line
e
m
s
m
e
s
e
$[2\bar{1}\bar{1}0]$
$[1\bar{1}00]$
$[\bar{1}\bar{1}20]$

Figure 2.3 The types of dislocation modes in the wurtzite structure (a) edge and (b) screw dislocation. Diagram (c) shows the line direction relation to Burgers vector[65].

The exact models in describing the generation of TDs are still contentious. Ning *et al*. has proposed that the formation of TDs is when the III-V nitride islands start to coalesce during the growth process[67]. If the crystal islands have coalesced with twisting (relative misorientations in the *c*-plane), screw dislocations can be created and similarly coalescence with some degree of tilting (relative misorientation along [0 0 0 1]), giving rise to edge dislocation, while the combination of both twist and tilt will generate the mixed dislocations. Then, thru further research via TEM, Wu *et al*. have embraced this island coalescence model[68]. However, Narayanan *et al*. provided proof against this model as they showed that there were already mixed and edge TDs on the clusters before they completely coalesced[69]. Alternatively, Narayanan proposed the creation of TDs was from the defects generates near the layer-substrate interface and does not generate at coalescence boundaries area. Oliver *et al*. also endorsed this model where the dislocation density at the coalescence boundaries was discovered to be consistent relative to the overall surface dislocation density[70].

2.3.3 Grain boundaries

The crystal grains boundaries are referred to as the grain boundaries defects and these types of defects can affect the electrical characteristics significantly. They can be exploited as carrier sinks or barrier transport depending on how the two crystal grains meet with relatively twist and/or tilt[71]. The small angle between the two crystal structures is caused by a small-angle grain boundary (SAGB) that form at the interface by a periodic pattern of dislocations. Here, the tilt angle θ is inversely proportional to the dislocation spacing[72].

2.3.4 Inversion domains and antiphase

Antiphase domains occur particularly when there is a shift in the crystal structure by an antiphase vector, **p**, with no twin formation. In the meantime, the inversion domain is produced if the two domain has a change in polarity direction, the opposite polarity between the domain boundary, presented in Figure 2.4. In III-V hetero-epitaxy growth on foreign substrates, this domain boundary is frequently noted.

On account of there is no center of symmetry in GaN crystal structure, the growth on the *c*-plane sapphire substrate of GaN epilayer may promote two kinds of polarities defined as [0 0 0 1] for Ga or [0 0 0 $\bar{1}$] for N. The GaN epilayers grown along the direction of <0 0 0 1> will obtain an alternating layer of Ga and N linked either by the single bond parallel to the growth direction or by the three bonds between these atoms (inclined toward the growth direction). Understandably, breaking the three bonds is much harder than a single bond. Hence, the growth polarity on the surface is determined by the atom with a single dangling bond pointing upward along the growth direction. The Ga-growth polarity becomes dominant if the growth direction pointing from Ga to N atom, whereas the N-growth polarity is dominant when the bond between N and Ga points towards the growth direction.

It is important to mention, the interpretation of “surface termination” that has regularly been used in some state-of-the-art may rather be uncleared depending on the growth condition (Ga-rich or N-rich), as the theoretical estimations and experimental findings demonstrate different surface reconstructions that results from the existence of Ga atoms. This has led to the formation of an adlayer which will change depending on the growth condition. This condition does not represent the growth polarity. Growth polarity seriously influences the chemistry and surface reconstruction of III-nitride growth. In terms of device performance, for instance, the piezoelectric field direction is determined by strain and as-grown epilayer polar direction[73]. Hence, a deep understanding of determining the mechanism of III-V growth polarity is of great significance.

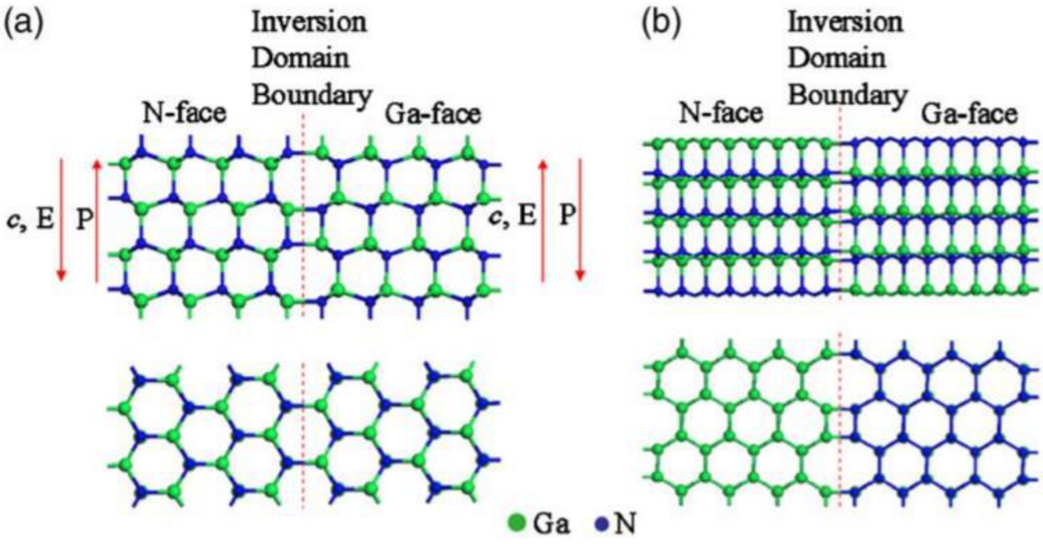

Figure 2.4 Inversion domain boundary in GaN[74]

2.4 Substrate materials.

In principle, the native substrate itself would be the best choice of substrates for the epitaxial growth of III-nitride elements. Regardless of the cost expensiveness, this is hardly ever approached because there are not commercially available on large scale with good crystal quality. While the production of GaN substrates via hydride vapor phase epitaxy (HVPE) has been immense in recent years, yet only a few reports on the substrates of AlN nor AlxGa1-xN with high Al percentage was found, even promising work on producing bulk AlN has been done at the early of 70’s[75]. So, foreign substrates were therefore been used in the growth of heteroepitaxial AlN and other III-nitride epilayers.

The type of substrates used in the epitaxy plays a crucial role in achieving high-quality crystal growth. To grow on it, the substrate should have comparable characteristics with the grown epilayer where it will determine the growth direction which influences the crystal orientation and/or structure. In AlN growth, for instance, grow on cubic substrates like (1 0 0) GaAs will orientate at cubic structure, while hexagonal is a form at hexagonal substrates like sapphire (Al_2O_3) with (0 0 0 1) planes. In normal practices, the lateral lattice parameter of the as-grown epilayer should have nearly the same as the substrate's interest. The defect density like threading and misfit dislocation will typically form at the interface if there is a mismatch in lattice parameter as well as when the epilayer is in a relaxation state. It is important to state that the strain in hetero-epitaxy III-nitride epilayers will continually be present due to the non-existence of perfect substrates[67], [76], [77].

The strain-induced during pseudomorphic growth become prevails especially at the early stages of crystal formation to match the substrate crystallographic. Besides being chemically stable, the substrate also should possess a relatively similar lateral TEC to correspond to the as-grown epilayers to avoid any plastic or elastic deformation which leads to cracking issues during the cooling period[41], [59]. Taking account of homogenous growth, lattice mismatch, strain, and surface mechanical properties of GaN crystal, it is best to choose GaN substrate for the growth of full LED.

2.5 Current techniques to grow III-V crystals.

In general, a high-quality and uniform growth of III-nitride epilayers has been an extensive study area that yields many growth methods, and all these methods fall into two main categories: physical vapor deposition and chemical vapor deposition. The selection of growth methods is crucial since different methods will affect the crystallinity, morphology as well as epilayer-substrate adhesion[78].

2.5.1 Plasma assisted molecular beam epitaxy (PAMBE)

The first system of molecular beam epitaxy (MBE) was developed for the GaAs epilayers growth by J. R. Arthur at Bell Laboratories[79] and been used later for devices fabrication by A. Cho[80]. It is now commonly used in the synthesis of small components like nanowires (NWs), quantum dots (QDs) as well as quantum wells (QWs) for different kinds of elements. Generally, the evaporation of desired elements includes the dopants that occurred in the MBE system was operated under ultra-high vacuum conditions. The evaporated atoms will only condense and epitaxially grow once it impinged on a perfectly heated substrate.

Plasma-assisted MBE (PAMBE) is the evolution of the MBE system and has been illustrated in Figure 2.5. It was designed with three chambers where each chamber has its pumping system and has been separated by a gate valve. The gate valve will only be opened once both chambers consume relatively the same level of pressure. First, the substrate has been load into the system through the introduction chamber where the pressure is drove down via ionic and turbo-molecular pumps (≈ 10−8 Torr). To limit air pollution, the chamber can only be opened under N_2 overpressure. Then, after being placed on a 2-inch sample holder of molybdenum (molyblock), the substrate was transported into the system by a cart. The cart will pass through the gate valve from the introduction chamber to the transfer chamber. Here, the transfer chamber pressure is drove down by an ionic pump (≈ 10−10 Torr). The substrates are stored here before the transfer arm is loading into the growth chamber.

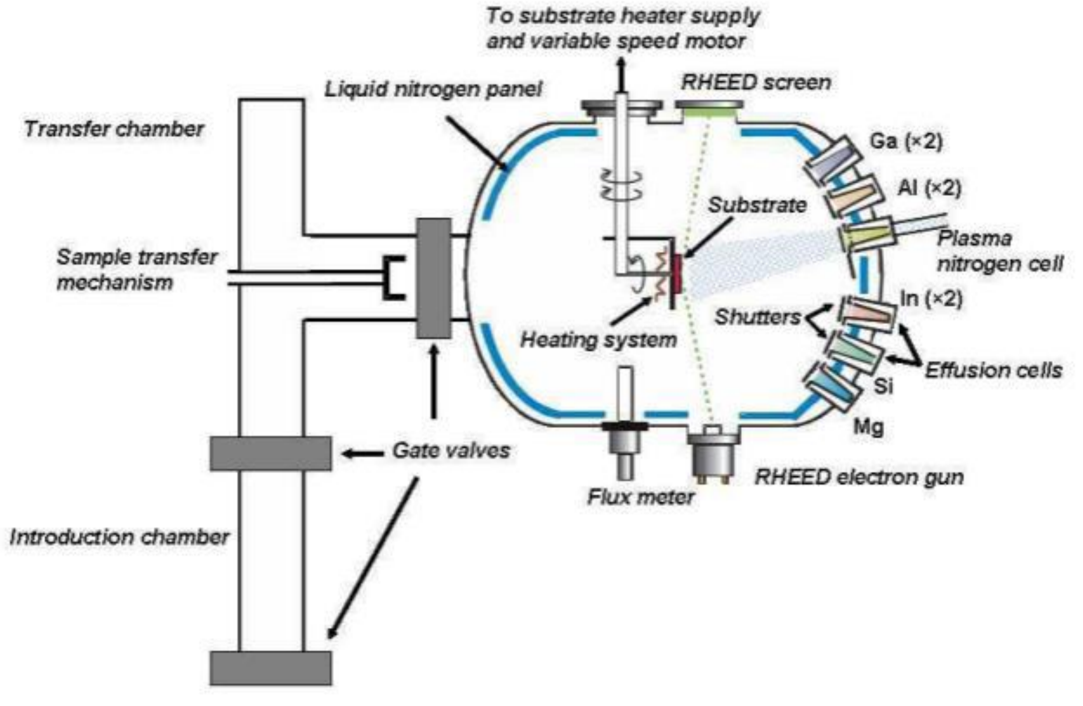
To substrate heater supply and variable speed motor
Liquid nitrogen panel
RHEED screen
Transfer chamber
Ga (×2)
Al (×2)
Substrate
Plasma nitrogen cell
Sample transfer mechanism
In (×2)
Shutters
Heating system
Effusion cells
Si
Mg
Gate valves
Flux meter
RHEED electron gun
Introduction chamber

Figure 2.5 The schematic diagram of PAMBE system[81].

2.5.2 Reactive magnetron sputtering

It has been testified that the secondary electron emission and the sputtering system have become one of the essential processes in a thin-film deposition. The creation of new ions will be occurred in the plasma glow by a collision of electrons with the ejected thin-film atoms. In the view of III-nitride growth by physical vapor deposition, reactive magnetron sputtering is the most promising system to be used.

Here, sputter yield (Y) is the most important parameter to describe the sputtering process and given by Mishin et al[82].

This system works by sputtering the compound target for the metal part while the nitride film will be formed by the corresponding reactive supplied gas, usually N_2. The system is typically subsisted by a chamber, gas inlet, vacuum pump, and power supply. In this close chamber, the susceptor (wafer holder) is placed at the bottom part while the deposition shutter and sputtering target are located at the top part. The nitrogen (N) and argon (Ar) gasses are fed into the inlet with the pump to retain the chambers in high vacuum conditions. Here, the power supply could be in radio-frequency (RF), direct-current (DC), or both. The electromagnetic waves from the cathode to the anode ring were transmitted by transferring a high voltage to the magnetron system. The gases inside the reaction chamber are converted into their plasma state in that phase. Ar followed by N_2 is supplied through the inlet into the chamber before ionized. The schematic diagram of an RF sputter is shown in Figure 2.6.

Generally, three sputterings of reactive DC, reactive pulsed DC, and reactive RF modes could be set depends on the type of power supply. In the DC mode, the anode and cathode (target) were supplied by positive and negative potentials, respectively. So, both gasses will float in the chamber with positive and negative ions. Then, the ions with positive charges are highly accelerated towards the group-III target disc and their atoms were ejected out the impact from this strong collision. Hence, the group-III and N ions will react under the “Poison condition” to produce the III-V elements. Finally, a thin film is formed on top of the substrate after these elements are condensed into a solid state[83]. It was noteworthy that reactive magnetron sputtering is useful for the low-temperature deposition of III-V elements with low impurity concentration and great uniformity. However, at a longer processing time, the elements will start to deposit on the side-wall of the chamber including the non-eroding areas of the target surface. The most serious disadvantage of reactive magnetron sputtering apart from having a small deposition rate is “arcing” as it can drastically restrict the process stability.

RF operates at 500 V with a power density of 10^{-20} Wcm^{-2}, its typical condition for magnetron discharging. However, the discharge may fall spontaneously into a tiny thread called an arc of ions and electrons. Such an arc discharge is defined by low voltage with a power density in the 10^{5} Wcm^{-2} range as the total power is focused on a very small target spot. The film growth may be contaminated by the particles produced by the arc. Heavy arcing can even destroy film-substrate interaction and the melting of the local target[84].

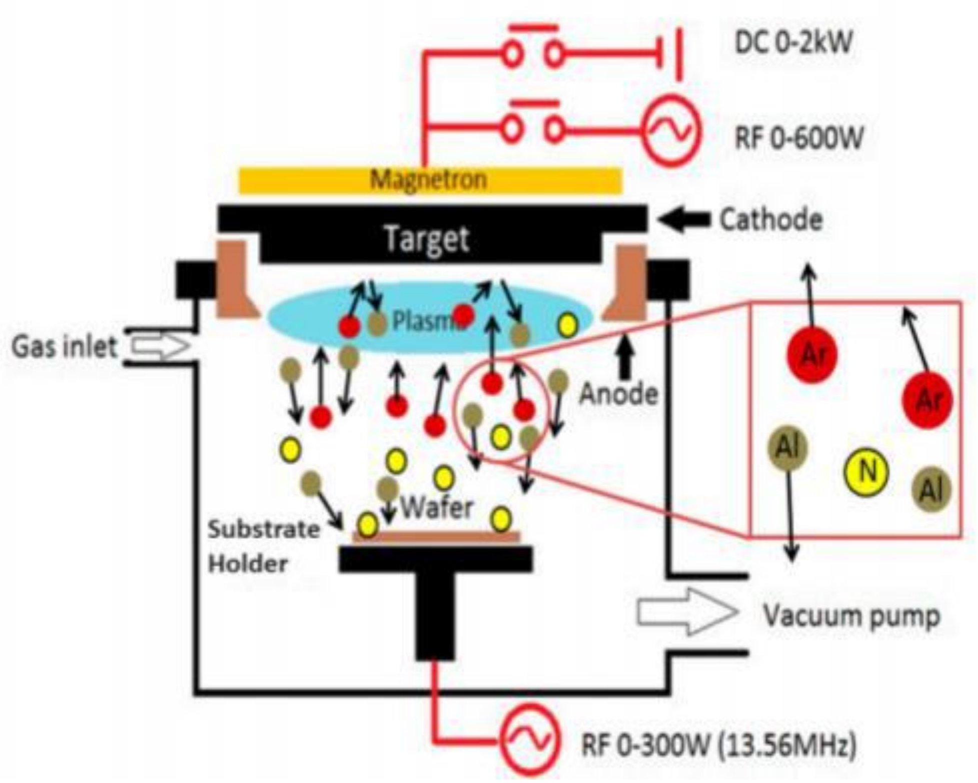
DC 0-2kW
RF 0-600W
Magnetron
Target
Cathode
Gas inlet
Plasma
Anode
Ar
Ar
Al
N
Al
Substrate Holder
Wafer
Vacuum pump
RF 0-300W (13.56MHz)

Figure 2.6 Schematic diagram of an RF sputter[85].